Article:

Wu, H. and Zhang, Y. (2026) A numerical investigation into the in-nozzle flow and near-field structure of flash-boiling ammonia sprays. International Communications in Heat and Mass Transfer, 172, Part 2. 110314. ISSN: 0735-1933

https://doi.org/10.1016/j.icheatmasstransfer.2025.110314

Highlights

A Numerical Investigation into the In-Nozzle Flow and Near-Field Structure of Flash-Boiling Ammonia Sprays

Haotian Wu, Yang Zhang

- Flare-flashing ammonia sprays (R_p=8) are 'choked' by a downstream shock wave, not at the nozzle orifice.
- A shock-induced, low-velocity core is identified as the primary mechanism driving the large-scale vortex structure.
- Provides a physical explanation for the characteristic "feather-shaped" spray morphology.
- Demonstrates how nozzle geometry (L/D, diameter) can be used to manipulate the shock structure and control atomization.
- In-nozzle phase change is suppressed at flare-flashing conditions, with the flow remaining subsonic at the nozzle exit

A Numerical Investigation into the In-Nozzle Flow and Near-Field Structure of Flash-Boiling Ammonia Sprays

Haotian Wu[a], Yang Zhang[a,*]

[a] *University of Sheffield, University of Sheffield, School of Mechanics, Aerospace & Civil , Sheffield, S10 2TN, UK*

Abstract

Ammonia is a zero-carbon fuel candidate, and flash-boiling atomization is an enabling technology for efficient combustion. While flash boiling produces complex spray structures, physical mechanisms governing the "flare-flashing" regime remain poorly understood. This study aims to identify the mechanism controlling spray structure and morphology in flare-flashing ammonia jets. Specifically, it investigates the role of compressibility and shock wave formation, which have not been previously identified as control elements. A two-dimensional simulation was established, coupled with the Homogeneous Relaxation Model (HRM) to simulate a non-equilibrium phase transition. The model was used to analyse the influence of nozzle geometry (L/D ratio, diameter) and operating conditions (pressure ratio, injection pressure) on in-nozzle flow and near-field spray development. The results revealed that the flow remains subsonic at the nozzle exit and is not choked at the orifice. It is 'choked' by a stationary, two-phase shock wave that forms in the near-field region downstream of the nozzle. This shock induces deceler-

*Corresponding author
Email address: yz100@sheffield.ac.uk (Yang Zhang)

Preprint submitted to International Communications in Heat and Mass Transfer *November 21, 2025*

ation at the spray's core, creating a velocity deceleration to the periphery, which drives a recirculating vortex, providing a physical explanation for the "feather-shaped" morphology observed in the experiments. It is concluded that the downstream shock wave is a mechanism controlling the structure and mass flow of flare-flashing sprays. This finding establishes a paradigm for injector design, offering a pathway to optimise fuel-air mixing.
Keywords: CFD, Ammonia spray, Flash boiling, Shock wave, Nozzle geometry

---

1. Introduction

Ammonia is increasingly recognised as a zero-carbon fuel alternative, driven by its proven production methods and the significant potential to reduce greenhouse gas emissions compared with fossil fuels when extracted from renewable resources [1], [2]. For efficiency considerations, ammonia is typically transported in liquid form during transportation processes because it has a higher energy density.**Due to the high saturation vapour pressure of ammonia under ambient pressure and high injection temperature, the spray of ammonia is often under superheated conditions. When burning ammonia, researchers found that heating liquid ammonia under pressure can bring its spray to a higher superheated state, where immediate and violent flash boiling can produce finer droplets, thereby achieving more stable combustion** [3].**Whereas complex spray structures and injector sizes prevent a non-intrusive method of experimental study [15], numerical simulation provides a cost-effective and efficient approach to investigate**

the detailed spray characteristics of flash-boiling ammonia sprays.

Flash-boiling represents a sophisticated evaporation process caused by a sudden pressure drop, and it is characterised by rapid phase transition in metastable liquids [4]. To describe the superheated degree, a ratio of saturated pressure at the initial fuel temperature over the ambient pressure is defined as the R_p. There are three different stages of superheated spray, namely non-flash boiling, transition flash boiling and flare flash boiling, depending on the morphology evolution. During the vigorous evaporation process of a metastable liquid, a discontinuity phenomenon is recognised as a shock wave [5]. Based on the evaporation wave theory, flashing sprays can trigger compressible phenomena such as shock waves and choked flow under rapid depressurising conditions [6]. The compressibility for flashing a two-phase mixture also differs from that of a single-phase fluid, which is often modelled with Wood's equation. The choking behaviour and shock waves are observed in various studies[6],[7], [8], [9], [10]. **Chen et al.[38] highlighted the need to understand the coupling between rapid phase change and shock wave interactions in flashing sprays. But the chocking behaviour at the boundary of flare flashing regimes (R_p ≈10)were not well investigated due to the huge density gradient at the near field for sprays between the transition regime and the flare flashing regime.**

Research indicates that flash-boiling is pivotal as it enhances atomisation and spray breakup, crucial processes for efficient combustion and optimal fuel utilisation [11], [12]. Extensive research has systematically investigated the detailed behaviours of flashing-boiling sprays across multiple dimensions. Liu et al. [11] researched single-hole ammonia spray characteristics, revealing macroscopic and microscopic behaviours at different flash boiling regimes. Complementary investigations by Pelé et al. [12] examined ammonia spray characteristics using contemporary gasoline direct injection (GDI) engine injectors. These studies highlighted the importance of injection parameters in determining flashing spray phase transition dynamics. **However, these observational studies could not resolve the underlying physical mechanism driving this specific structure. The reasons of the 'bell' shaped spray morphology at near-field and the 'feather' shape during early injection remains unknown in the field.**

Additionally, the geometric configuration of nozzle systems also emerges as a particularly crucial factor influencing spray characteristics. The relationship between cavitation and spray has also been reviewed [13]. Li et al. [14] examined the near-field and far-field ammonia flashing spray characteristics. Colson et al. [15] conducted a comprehensive experimental study examining the intricate relationships between injection temperature, nozzle geometry, and flashing transition dynamics. Fang et al. [16] discovered that flashing liquid ammonia would have a resistance phenomenon under high superheated conditions in a diesel injector at 100 MPa injection pressure. Wang et al. [13] conducted research investigating cavitation enhancement in two-dimensional slit nozzles, revealing unclear interactions between real nozzle geometry and phase transition phenomena. Although this phenomenon was explained by the unsteady cavitation bubble, these studies still indicate that minute variations in nozzle design could substantially alter spray formation mechanisms, emphasising the need for precise geometric optimisation.

Numerical research of ammonia flashing spray was primarily simulated with two methods: the Lagrangian method and the Eulerian method. For combustion simulation, the Lagrangian method proves to be more computationally efficient and can be coupled with species transportations in diffusion combustion [17], [18], [19]. However, due to different breakup mechanisms, none of the current injection models can fully recreate the spray morphology of flashing ammonia spray [20]. On the other hand, the homogeneous relaxation model (HRM), established by Downar-Zapolski et al. [29], provides an empirical equation to calculate the phase transformations source terms. Additionally, the Eulerian framework and HRM have proven effective in simulating flash-boiling sprays and nozzle cavitation, offering insights into phase transitions and spray dynamics [21], [22], [23], [24]. Guo et al.[9], [24], [21] numerically investigate the dynamics of under-expanded and flash boiling jets in multi-hole gasoline direct injection (GDI) systems, focusing on jet development, jet-to-jet interactions, and spray collapse mechanisms. Using simulation and experimental techniques, the studies analyse how fuel properties, flash boiling, expansion ratio, injection pressure, and ambient conditions influence jet morphology, shock structures, and flow choking. Key findings reveal that phase change and inertial forces critically shape shock cell structure and spray collapse, with parameters like relaxation time, expansion ratio, and phase change effect and inertial effect governing the behaviour and interactions of flashing jets. The relation found is that thermal and fluid dynamic factors co-determine jet structure, collapse, and shock formation. Lyras et al.[25] conducted coding and numerical application with the HRM model. Complementary research by Gärtner et al. [22], [23] offered numerical and experimental analyses of flashing cryogenic jets, further validating these methodologies. These studies collectively demonstrated the reliability of the compressible two-phase method in shock wave simulation.

Previous numerical studies have primarily focused on the ammonia external spray morphology, but not on the in-nozzle cavitation and shock wave. **The authors identified that different nozzle configurations and in-nozzle flow behaviours, external spray morphology and shock waves are highly relevant.**This study aims to identify the mechanism controlling spray structure and morphology in flare-flashing ammonia jets through a comprehensive numerical investigation of ammonia spray dynamics. The specific research objectives include investigating cavitation within the nozzle, evaluating the critical impact of nozzle orifice geometry, examining the effects of injection parameters on spray characteristics outside the nozzle, and characterising shock wave formation. This study utilised a compressible VOF solver based on OpenFOAM to examine the influence of cavitation and compressibility on spray parameters under different nozzle designs, injection pressures, and superheated indices. This work contributes to the optimisation of clean ammonia combustion by enhancing our understanding of ammonia flash-boiling cavitation and its effects on spray behaviour.

2. Methodology

2.1. Governing equations

This paper builds the CFD simulation based on the code of Gärtner [22] on OpenFOAM, a compressible VOF solver with the HRM to simulate phase changing. The turbulence model used here is k-ω SST, and the transportation equations of mass, momentum and volume fraction follow the one-fluid approach, while the energy conservation was solved separately for each phase connected by source terms:

$$\frac{\partial \bar{\rho}_L \tilde{\alpha}}{\partial t} + \partial \bar{\rho} \tilde{\alpha} \tilde{\mathbf{u}} + \nabla \cdot \left(\overline{\rho \alpha" \mathbf{u}"} \right) = \tilde{\dot{m}}_L \tag{1}$$

$$\frac{\partial \bar{\rho} \tilde{\mathbf{u}}}{\partial t} + \nabla \cdot \left(\bar{\rho} \tilde{\mathbf{u}} \tilde{\mathbf{u}} \right) = -\nabla \bar{\rho} + \bar{\rho} g + \nabla \cdot \tilde{\tau}_{\mathbf{t}} \tag{2}$$

$$\begin{aligned} \bar{\rho} \left(\frac{D\tilde{h}_L}{Dt} \right) + \bar{\rho} \left(\frac{D\tilde{K}}{Dt} \right) = & \left(\frac{\partial \bar{p}}{\partial t} + \nabla \cdot \left(k_{L,EFF} \nabla \tilde{T}_L \right) \right) \\ & + \frac{\bar{\rho}}{\bar{\rho}_L \tilde{\alpha}_L} \dot{m}_L \left(h_{SG}\left(p\right) - \tilde{h}_L \right) \end{aligned} \tag{3}$$

$$\begin{aligned} \bar{\rho} \left(\frac{D\tilde{h}_G}{Dt} \right) + \bar{\rho} \left(\frac{D\tilde{K}}{Dt} \right) = & \left(\frac{\partial \bar{p}}{\partial t} + \nabla \cdot \left(k_{G,\mathrm{EFF}} \nabla \tilde{T}_G \right) \right) \\ & + \frac{\bar{\rho}}{\bar{\rho}_G \tilde{\alpha}_G} \dot{m}_L \left(\tilde{h}_G - h_{SG}\left(p\right) \right) \end{aligned} \tag{4}$$

where $\mathbf{u}$, K, τ_t, h, k_{EFF}, g, α are the velocity vector, kinetic energy, turbulent viscous stress tensor, enthalpy, effective thermal conductivity, gravity and liquid volume fraction, respectively. The overbars, tildes and double prime represent the Reynolds averages, Favre averages and fluctuations, respectively. Subscripts 'L', 'G' are denoted as liquid and vapour properties, while 'SL' and 'SG' are denoted as saturated properties for liquid and vapour phase. The mixture properties are calculated by volume averaging and written without any subscripts. The effective thermal conductivity k_{EFF} is calculated as the sum of laminar and turbulent conductivity. The turbulent conductivity

$$k_t = \rho \frac{\nu_t}{Pr_t} \tag{5}$$

where the Pr_t is the turbulent Prandtl number, which is set to 1.0 in this study. A gradient diffusion assumption is used here cite anez2019:

$$-\nabla \cdot \left(\overline{\rho\alpha"\mathbf{u}"}\right) = \bar{\rho}_L \nabla \cdot \left(\frac{\nu_t}{Sc_t} \nabla \tilde{\alpha}_L\right) \tag{6}$$

where ν_t is the turbulence viscosity and Sc_{t} is the turbulent Schmidt number. Linear pressure and density relationship is assumed as $\rho = \rho_0 + \psi p$, where the compressibility is defined according to [27]:

$$\frac{\partial \rho}{\partial p} = \sum_{i=1}^{N} (\rho_i \alpha_i) \sum_{i=1}^{N} \left(\frac{\alpha_i}{\rho_i} \left(\frac{\partial \rho}{\partial p}_i\right)\right) \tag{7}$$

The mass and momentum equations formulate the pressure equation,

$$\nabla \cdot \left(\frac{\nabla p}{a_p}\right) - \nabla \cdot \left(\frac{H(\mathbf{u})}{a_p}\right) = \frac{1}{\rho} \frac{D\rho}{Dt} \tag{8}$$

The H(u) and a_p represent the momentum equation's off-diagonal terms and diagonal terms. The material derivative of density consists of the mixture compressibility, which is expressed in equation (7). Therefore, the mixture sonic velocity, which is the inverse of compressibility, becomes surprisingly low when the volume fraction is not close to uniform or 0 [28]. This is also the critical feature of the shock wave structure inside the ammonia spray. The homogeneous relaxation model (HRM) is applied as the phase change model in this paper. According to Downar-Zapolski[29], the empirical correlation of evaporating time and non-equilibrium evaporation rate is defined as:

$$\frac{D\chi}{Dt} = -\chi \frac{h_L - h_{SL}}{h_{SG} - h_{SL}} \frac{1}{\Theta} = \frac{\dot{m}_L}{\rho} \tag{9}$$

With the $\bar{\chi}$ being the equilibrium and χ being the instantaneous mass fraction, where time scale θ is defined as:

$$\theta = \theta_0 \alpha_v^{-0.54} \varphi^{-1.76} \tag{10}$$

$$\alpha_v = \left(\frac{\rho_L - \rho}{\rho_L - \rho_v}\right) \tag{11}$$

$$\varphi = \left(\frac{p_s\left(T\right) - p}{p_c - p_s\left(T\right)}\right) \tag{12}$$

Where θ_0, -0.54 and -1.76 are empirical parameters and were determined to be in Downar-Zapolski et al. [29]. Reliability of these model constants on ammonia is examined by experimental study and sensitivity test in the following sections. In equation (12), p_s stands for saturation pressure and p_c stands for the critical pressure of the fluid.

2.2. Numerical setup

The numerical domain is built according to the nozzle geometry and parts of the outside chamber in the experiments of Colson et al. [15]. The inner diameters of the injector and the nozzle orifice are 5mm and 0.21mm, respectively, connected by a 120-degree cone with a rounded corner, whose radius is 0.1 mm at the orifice inlet.

The numerical cases in this paper are built in 2D, including the nozzle inner flow area and part of the outside chamber. In Figure 1, the symmetric domain built outside the nozzle is 17mm in length and 9mm in width, with the symmetric axis at the zero position of the x-axis. Boundary conditions for the inlet, outlets, and walls are also noted in Figure 1. Detailed nozzle geometry information of different cases is listed in Table 1. The injection was simplified to a fixed injection pressure, without considering the effect of needle movement. The instantaneous solutions are calculated in this study, and the following results are compared at 0.01 s. To compare the effect of initial temperature, nozzle L/D ratio and orifice diameter on spray parameters, 5 cases were selected for validation from the experiments of Colson et al.[15]. Furthermore, cases with more injection pressure and less ambient pressure were also built and discussed in a later section of this paper. This study is based on OpenFOAM, and the VOF compressible phase change solver with HRM model is built by Gärtner et al. [22]. The initial time step size is set to 6e-09s for stabilising the simulation, and an adaptive time step size is used. Additionally, the PIMPLE algorithm is applied with three outer iterations to make the equation calculation converge. All the simulations are calculated

Cases	1	2	3	4	5
Injection temperature (K)	270	295	292	291	279
R_p	3.8	9.0	8.2	7.9	5.2
Injection pressure (Pa)	8.7e+05	10.1e+05	10.9e+05	10.1e+05	9.6e+05
Nozzle aspect ratio	10	5	10	10	10
Nozzle diameter (mm)	0.21	0.21	0.21	0.15	0.21
Θ_0	1e-07	1e-04	3.87e-07	2e-07	2e-07
Flashing stage	Partial flashing	Non-flashing	Fully flashing	Fully flashing	Partial flashing

Table 1: Injection conditions and empirical constant for different cases.

under 1e-05 Pa and 298 K ambient conditions. The time scale θ_0 was modified for case 1 (1e-04) and 2 (1e-07) [30] to fit the experimental results—the original constant works well with case 3 in this study. The mesh is displayed below in Figure 2. The grid-independent test was done to reduce the mesh sensitivity of the results. Three sizes of mesh were made with 37K, 48K and 106K of cells. Figure 3 shows the liquid volume fraction plot under different mesh numbers. There is not much difference that can be found regarding the axial and radial distribution at the nozzle exit. The refinement of the orifice area leading to the 106K mesh cells is necessary for a higher resolution of the variable field inside the orifice.

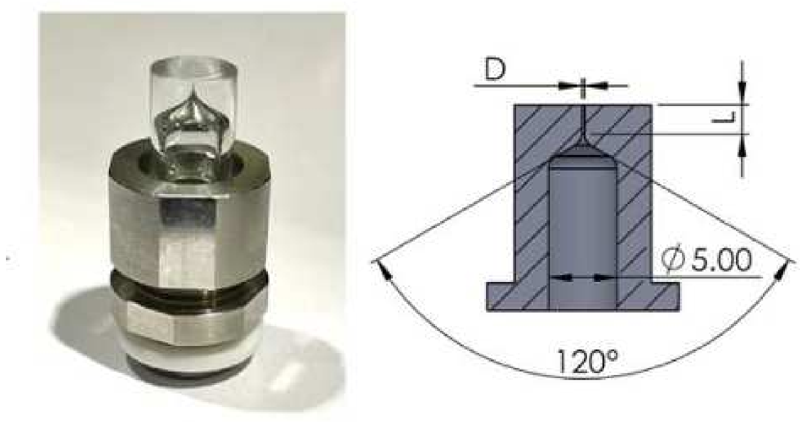

Figure 1: Nozzle inner geometry in the experiment of Colson et al.[15].

3. Results and Discussion

3.1. Validation

Colson et al. [15] conducted an experimental study on ammonia spray at varying superheated degrees and ratios of nozzle orifice length to diameter. In their experiments, case 1 did not flash at all, case 2 and 5 belonged to the transient flashing regime, and case 3 and 4 were fully flashing [15]. **In the numerical study, the spray boundary was determined by the most significant gradient of liquid phase mass fraction.The comparison between the experimental and numerical spray angles can be found in Figure 4 with all the cases staying in the error range. From Wang's study previously, the time scale constant in the HRM**

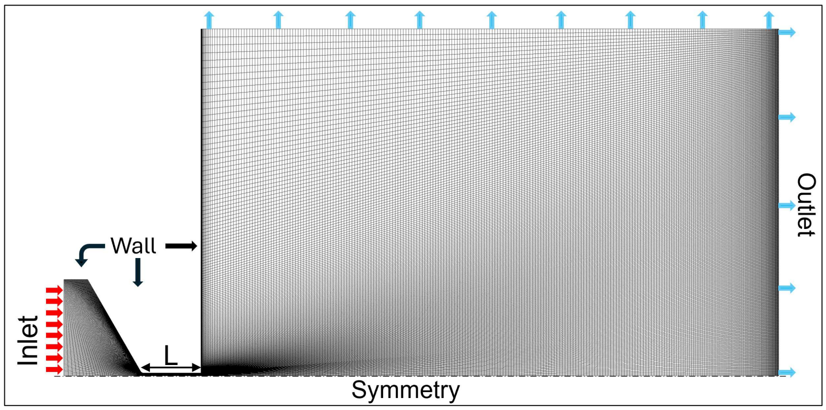

Figure 2: Mesh and boundary of the 2D simulation domain (chamber domain length = 17mm).

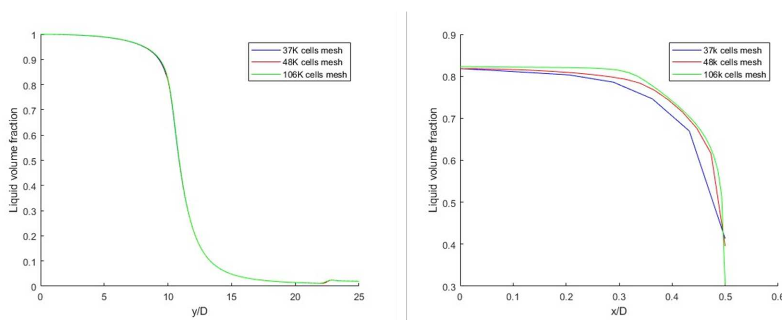

Figure 3: Liquid volume fraction profiles at (left) axial position where $x/D = 0$ and (right) radial position where $y/D = 10$ with three different mesh resolutions.

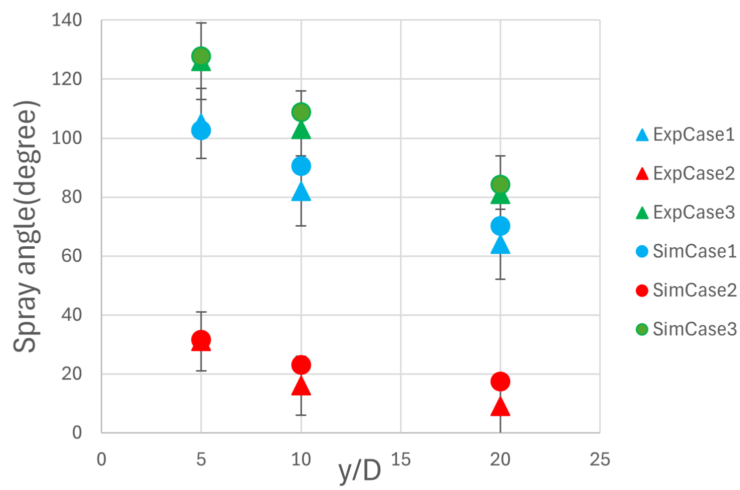

Figure 4: Spray angle validation at normalised axial position (5,10, and 20 times of nozzle diameter) compared with experimental results from Colson et al.[11] for cases 1 to 3.

model needed to be modified to be 1e-07 and 1e-04 for better angle predictions in cases 1 and 2 [30]. Additionally, sensitivity tests on time scale constant θ_0 were taken regarding cases 4 and 5. In Figure 5 for cases 4 and 5 at the near field 5D, the simulation shows a discrepancy compared to the experimental results with different θ_0 due to the small diameter of case 4 (0.15mm) and the transition flashing behaviour of case 5. It is explained in Gartner et al.[22] that the model used in this study is valid for full flashing flow under high pressure. Therefore, for case 3 with the highest injection pressure and fuel temperature, the correlation has the best prediction without any adjustment. In Figure 5, the lateral spray angle may be lower than observed in experiments due to the neglect of the aerodynamic breakup effect. Therefore, the authors consider the near-field angle to be more significant for selecting the coefficient in the simulation. However, the consistency of experimental results and the numerical results is not perfect when $\theta_0 = 2 \times 10^{-7}$; the near field prediction was the closest to Colson's results. In Figure 5 (b), it is clear that when the θ is chosen to be 2×10^{-7}, the spray angle predictions are much closer. It can be found that, for non-flashing, partial flashing conditions, the evaporation time scale is over-predicted and under-predicted, respectively, for the original HRM model[29]. However, for flare flashing sprays, the model performs well except when the nozzle diameter is low (0.15mm). This demonstrates that the empirical correlation of the HRM model can be further improved for ammonia, but the overall prediction of spray cone angle is acceptable with the modification.

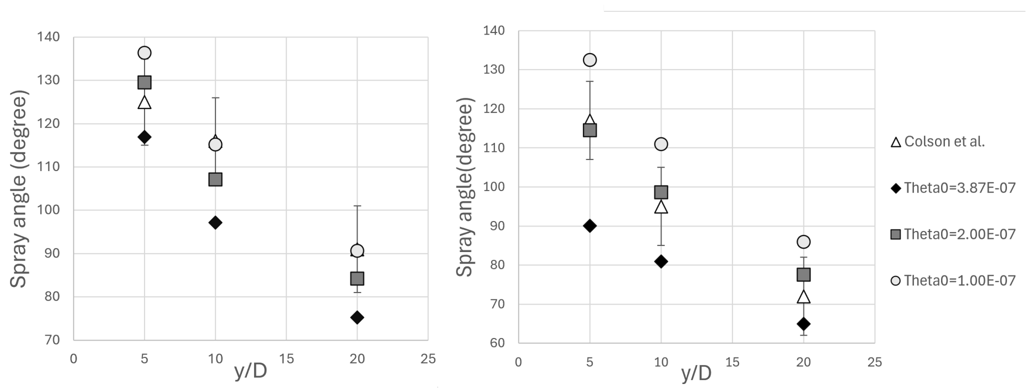

Figure 5: The influence of the empirical flashing time constant in Downar-Zapolski [29] HRM model on the spray angle for cases 4 (left) and 5 (right), validated with Colson's results[15].

3.2. Distribution of spray parameters

Figure 6 gives a comprehensive description of the spray parameters. For the flashing sprays, a first acceleration and depression happen inside the

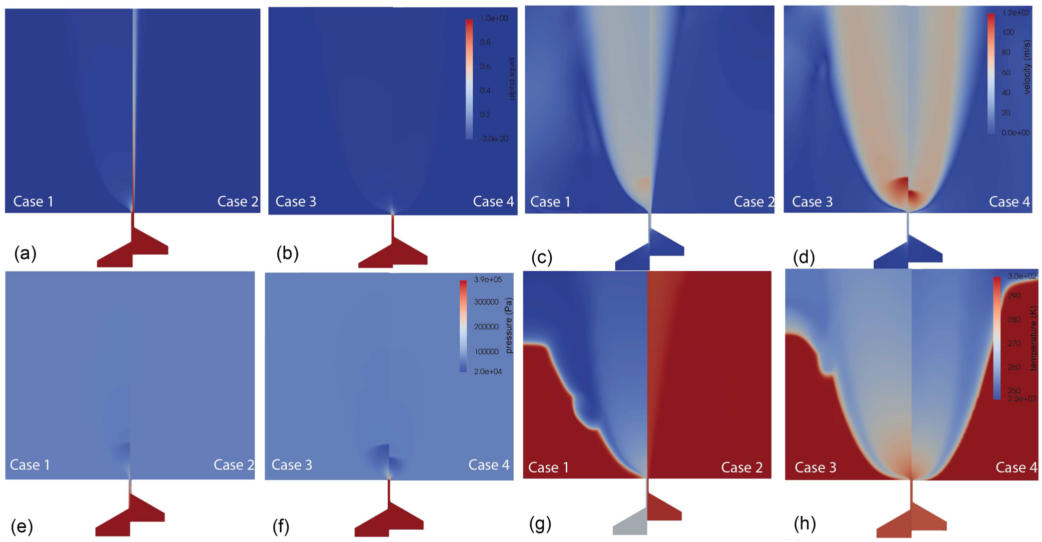

Figure 6: Distribution of (a-b) liquid volume fraction (c-d) velocity (e-f) pressure (g-h) temperature for different L/D ratios: case 1 $R_p = 3.8, L/D = 10$ to case 2 $R_p = 9.0, L/D = 5$, and different diameters: case 3 $R_p = 8.2, D = 0.21$ to case 4 $R_p = 7.9, D = 0.15$.

nozzle, which gives the liquid fuel momentum and bubble nucleation. Then the spray has a second depression outside the nozzle, while the liquid phases undergo a flashing evaporation, expanding the spray angle and evaporating quickly. The liquid phase quickly breaks down into small droplets outside the orifice exit. Then, the accelerating droplets cool down and stop flashing due to high latent heat. The normal shock wave formed inside the spray hinders the central mixture momentum, thus the spray near-field morphology became a 'bell' shape. For cases where the nozzle L/R ratio is 5 and 10, the spray exhibited a different flashing stage between non-flashing and flare flashing. For two different nozzle diameters, the spray expanded less in volume. For other initial temperatures (case 1 and case 3), the spray follows the transition flashing behaviour and flare flashing behaviour. Generally, the morphology is similar to the experimental results in Colson et al. [15]. **The temperature field shows that the liquid phase cools down near the boiling point at the spray edge during the flashing process. Surprisingly, the temperature is higher for case 3 due to a higher initial temperature, which indicates a more violent flashing evaporation. This is also consistent with the higher void fraction found in case 3.**

According to equation (9), the flash boiling evaporation time scale constant $/theta_0$ is partially determined by local pressure. During the flash boiling, the expansion stimulates the evaporation through local static pressure, while the evaporation causes the expansion. The liquid and vapour mixture will eventually cool down to its boiling point or meet the local sound speed.

3.3. The influence of superheated and nozzle parameters

3.3.1. In-nozzle axis distribution

An analysis of the internal nozzle flow is essential to understand the initial conditions that govern downstream spray development. Figure 7(a-c) presents the axial profiles of key flow parameters inside the nozzle for all simulated cases. The pressure profiles in Fig. 7(a-b) reveal that for the flashing cases (1, 3, and 4), the static pressure drops below the corresponding saturation vapour pressure. This indicates that the liquid ammonia enters a metastable state within the nozzle orifice, a prerequisite for flash boiling. The observation that the total pressure is approximately the sum of the static and dynamic pressures for a significant portion of the nozzle length suggests the flow remains largely incompressible before the onset of significant phase change. However, for cases 1, 3, and 4, the decrease in total pressure near the nozzle outlet indicates the beginning of two-phase compressible flow. In con-

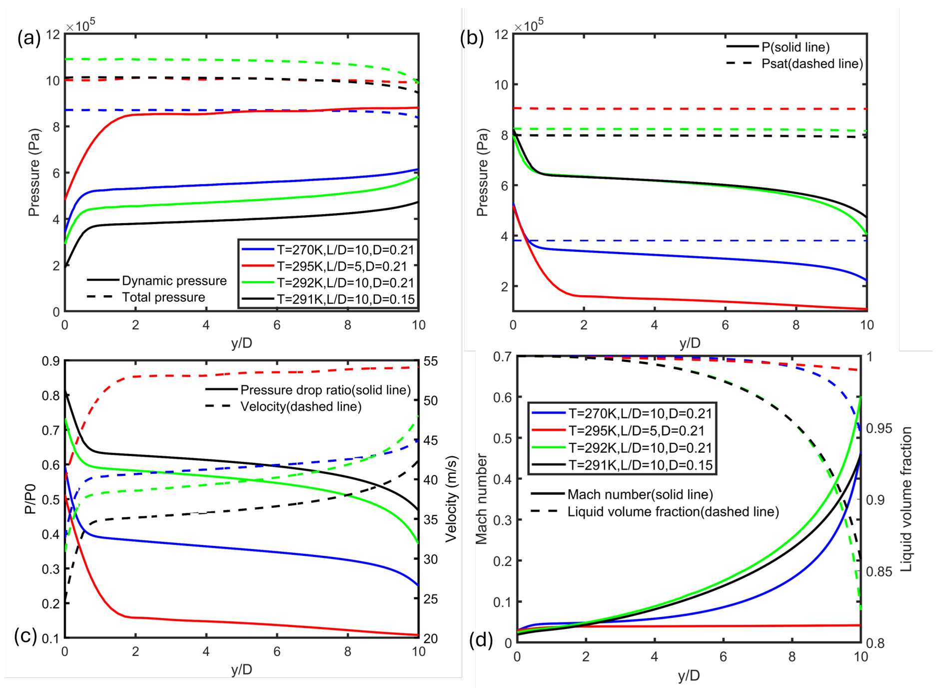

Figure 7: Parameters plotted over the nozzle axis: (a) Total pressure and Dynamic pressure, (b) Static pressure and Saturation vapour pressure, (c) Velocity and pressure drop ratio, (d) Mach number and liquid volume fraction.

trast, the profiles for case 2 with lower L/D are consistent with single-phase, non-flashing behaviour. **It is considered by the authors that for the shorter nozzle orifice, due to the hydraulic flip caused by cavitation inside the nozzle, which stabilised the in-nozzle flow leading to less turbulence interaction and less nucleation of small bubble. Therefore, the whole flashing process did not happened like a 'shaken soda water', instead, followed the heterogeneous nucleation process which have a mild vaporisation rate.**Notably, even when the static pressure is below the vapour pressure, significant flash boiling does not occur within the nozzle orifice for cases 1, 3, and 4. This phenomenon, where phase change is suppressed, aligns with experimental findings by Wang et al. [13]. They proposed that bubble growth is hindered by in-layer forces, turbulence, and the physical constraints imposed by surrounding bubbles within the confined orifice.

The degree of in-nozzle phase change is strongly influenced by both the nozzle geometry (L/D ratio) and the operating conditions (R_p, injection pressure). The axial profiles of liquid volume fraction, Mach number, and velocity are presented in Fig. 7(c-d). The calculation of the two-phase Mach number required different approaches depending on the flow regime: for the flashing cases (1, 3, and 4), the model is based on Nguyen [28], which is a function of volume fraction, phase density, and the adiabatic sonic velocity for each phase. For case 2, a volume-fraction-averaged sound speed was found to be more suitable. A comparison between case 2 and case 3, which have similar R_p values, shows that evaporation is negligible in case 2. This is attributed to its low L/D ratio (¡ 5), which limits the residence time for bubble nucleation and growth, a conclusion supported by the work of Wu et al. [33]. Consequently, the characteristic two-stage depressurisation of superheated sprays does not occur in case 2. In addition to the aspect ratio, the nozzle diameter itself is influential. Our results show that, unlike a single-phase jet, a larger diameter can cause a more significant pressure loss at the nozzle inlet, leading to a higher outlet volume flow rate; this feature is also observed experimentally by Zhong et al. [32]. Furthermore, a comparison between the void fraction plots of cases 4 and 3, which share the same R_p and L/D and are simulated with different time scale constants in the HRM model, reveals that the evaporation time constant can be the key difference between flashing sprays in different nozzle diameters.

3.3.2. Out-nozzle axial distribution

Upon exiting the nozzle, the mixture, which was established to be subsonic, undergoes a dramatic transformation in the near-field region as shown by the axial profiles in Figure 8. The flashing cases (1, 3, and 4) experience a vigorous depressurisation process as the fluid expands into the low-pressure ambient environment (Fig. 8(a)). This rapid expansion, fuelled by the intense phase change, converts thermal energy into kinetic energy, accelerating the axial flow significantly (Fig. 8(b)). The combination of this thermal acceleration and the initial exit momentum causes the mixture to exceed the local speed of sound, forming a characteristic under-expanded supersonic jet. This supersonic region, where the static pressure falls well below the ambient back pressure, is visible for the flashing cases, extending from approximately 4D to 13D downstream.

The subsonic exit condition confirms that the flare flashing jet is not

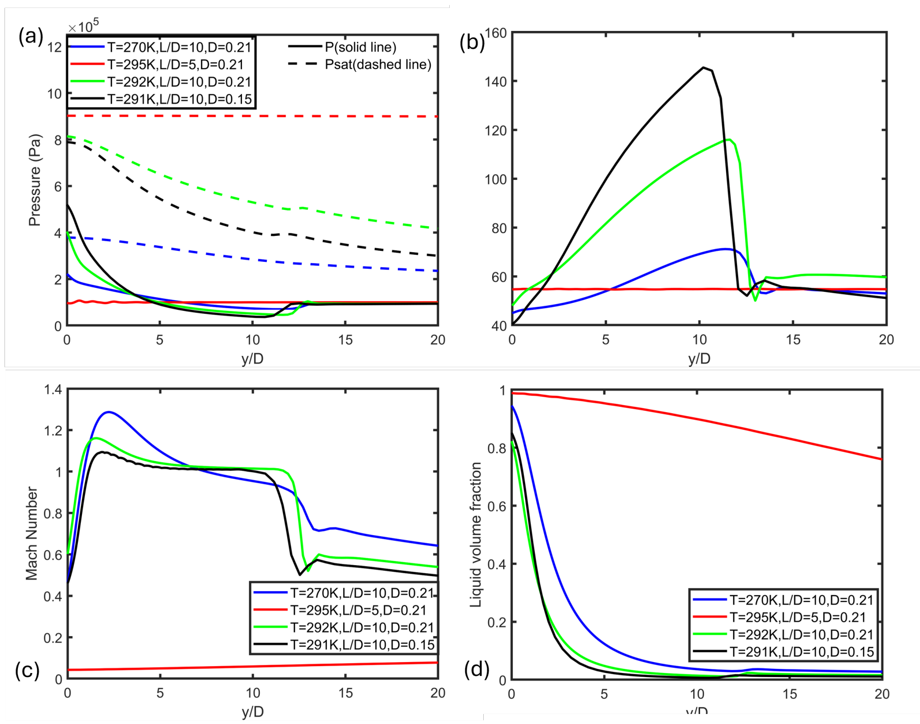

Figure 8: Parameters plotted on axial line outside the nozzle: (a) Static pressure and ammonia saturation pressure,(b) Velocity,(c) Mach number, (d) Liquid volume fraction.

choked at the orifice. Instead, we propose that the flow is hydrodynamically 'choked' by a stationary shock wave that forms downstream. This shock wave is evidenced by the abrupt pressure rise and the corresponding sharp deceleration of the flow shown in Fig. 8(c-d). After passing through this shock, the mixture becomes subsonic again, and the pressure begins to recover towards the ambient level. This downstream shock structure, rather than the physical nozzle throat, is what ultimately limits the mass flow rate for the flare flashing regime under these conditions. This mechanism explains the lower-than-expected outlet velocity in cases like case 3, where intense flashing might otherwise be expected to produce even higher speeds.

A comparison of the cases in Figure 8 provides further support for this mechanism. While under similar injection conditions, case 4 accelerates more rapidly and reaches a higher peak velocity than case 3. It is speculated that with a smaller nozzle diameter, the pressure gradient between the nozzle upstream and nozzle orifice is smaller. In contrast, the gradient between the nozzle exit and the ambient environment is steeper, resulting in more intense bubble breakup and evaporation immediately upstream of the shock wave, a finding consistent with Zhong et al. [32]. For the partial flashing spray (case 1), the vaporisation process is slower, providing less energy for expansion and resulting in a weaker acceleration. Notably, while the pre-shock velocities differ significantly across the cases, the post-shock velocities at the centre converge to a similar magnitude, suggesting the shock wave acts as a primary determinant of the subsequent downstream spray centre momentum. This can be explained by the similar injection pressure and ambient conditions in the current cases.

In the near-nozzle region, the expanding and evaporating two-phase mixture can lead to the formation of a normal shock, resulting in a sharp axial velocity reduction downstream. While the axial flow experiences this significant deceleration, the radial velocity, primarily driven by the expansive forces of flash boiling, typically does not reach the local speed of sound at low superheat degrees (low R_p) during flare flashing. Consequently, the central axial velocity of the spray after the shock wave becomes lower than the surrounding flow, contributing to a wider spray angle in the near field. This phenomenon also accounts for the characteristic vortex structures observed during the flare flash boiling stage. The temporal evolution of these large vortices, alongside the lateral shrinking of the single spray liquid plume observed in morphology studies, is governed by the velocity and pressure differentials between the central and radial mixture flows during flare flashing. Furthermore, experimental results indicate that, consistent with findings by Zhong et al. [32], the presence of the two-phase shock indeed hinders axial momentum transmission. However, the radial velocity does not attain the same Mach number. This complex interplay results in a "feather-shaped" spray morphology, characterised by initial expansion followed by vortex formation and subsequent spray shrinking. At high superheat degrees (high R_p), the surrounding flow exhibits greater displacement, either travelling axially or creating a recirculating area. It is also observed that a reduction in ambient pressure does not further increase the flare flash boiling tip speed [16], owing to choking occurring within the spray centre. In contrast to flare flashing, partial flashing sprays exhibit a higher axial velocity, indicating a less compressible two-phase mixture. However, Case 1 under partial flashing conditions demonstrated a higher Mach number both upstream and downstream of the shock. This is attributed to the lower fuel temperature leading to a reduced local speed of sound (Figure 8). In the model utilised in this study, the influence of decreased sound speed on the Mach number was found to be more significant than differences in local flow velocity, highlighting a critical aspect for model refinement.

For case 2 in Figure 9, the flashing process is barely happening, while surface evaporation is dominating. For the other cases, the effect of superheat degrees can be observed, where case 1 evaporates much more slowly than the others. During the travelling of the spray, the evaporation rate slowly dropped when the evaporation is generally stabilising. Over the selected axial position, the temperature reduction is the highest for case 4, due to the high superheat degree and small nozzle diameter. This also indicates that a small nozzle diameter can induce a more violent nucleation process, enhancing the more intense bubble breakup and evaporation process mentioned earlier. The axial temperature profile in Figure 9 provides additional thermodynamic evidence for the shock structure. During the initial expansion, the mixture temperature decreases sharply due to the latent heat of evaporation. However, as the flow traverses the shock wave, it is rapidly compressed, causing the local temperature to increase slightly due to compressive heating before continuing its gradual decrease. This distinct temperature rise precisely at the location of the pressure jump and velocity drop offers evidence for the existence and location of the two-phase shock wave. **The lateral distribution of temperature for case 1,3, and 4 is**

shaped like a 'W' similar to Wang et al. [30]'s simulation result and verified in Zhou et al. [37] experimental measurement of flashing temperature field. It is worth noting that temperature values here are mixture temperatures therefore influenced by the droplet temperature except for the outside diluted part. This explains the 'W' shape in the lateral plot: in the centre of the spray, droplets are surrounded by saturated cold vapour, which slows down the process of evaporation. Meanwhile, on the edge of the spray, droplets are having a great shearing movement and also turbulence mixing with the ambient gas. The droplet surface would have a larger temperature and vapour pressure difference compared with the ambient conditions. Furthermore, the secondary breakup effect can increase the droplet surface area, causing the temperature to be significantly lower than the centre.

Previous study on shape of the flashing spray [7], demonstrates a characteristic radial velocity distribution where the highest velocities are concentrated at the jet's periphery, similar to observations in cases 3 and 4 in Fig. 6. This peripheral velocity emphasis was also reported by Wu et al. [33] at $R_p = 10$ for flashing sprays. They noted that the spray structure resembled that of a pressure-swirl atomiser, characterised by higher radial droplet velocities at the periphery than at the centre, and a negative pressure zone in the core that induces a circulated flow. In this study, this characteristic is attributed to the resistance generated by the two-phase compression shock wave at the spray centre. Experimentally, at low R_p conditions, visualising this shock wave is challenging using methods like schlieren or Diffuse Backlight Illumination (DBI). This difficulty arises because the dense liquid-gas mixture within the spray plume obscures the shock wave. Although the underlying atomization physics differ fundamentally, the observed congruence in flow patterns corroborates the theory of an internal normal shock wave within the spray.

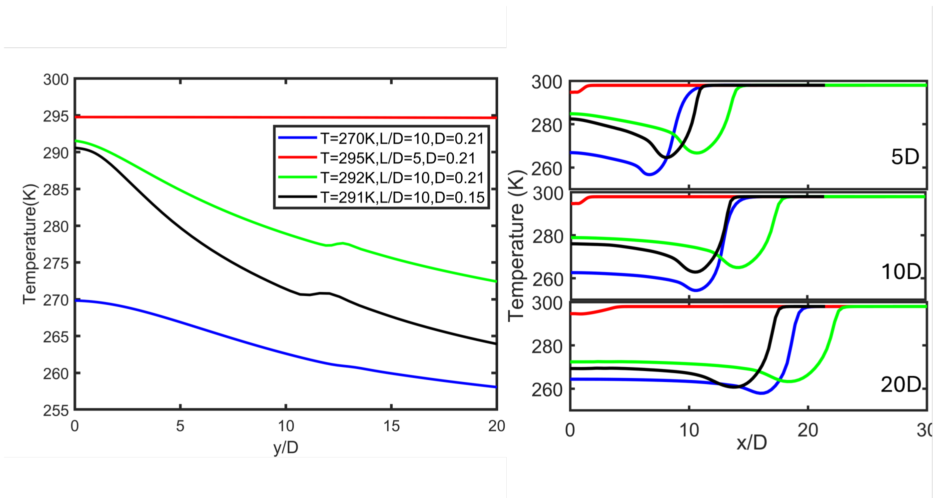

Figure 9: Temperature profile of spray parameters outside nozzle at axial location (left) and lateral location on 5D, 10D and 20D locations (right)

to

3.3.3. Out-nozzle radial distributions

Figure 10 to 12 present the radial distributions of velocity, pressure, liquid volume fraction, and Mach number at downstream locations of 5D, 10D, and 20D, respectively. At the 5D location (Figure 10), the analysis reveals that the evaporation process is not yet fully initiated for Case 1, as evidenced by a significant liquid core. In contrast, the liquid volume fraction for Cases 3 and 4 is already below 0.1. For all three flashing conditions, the liquid

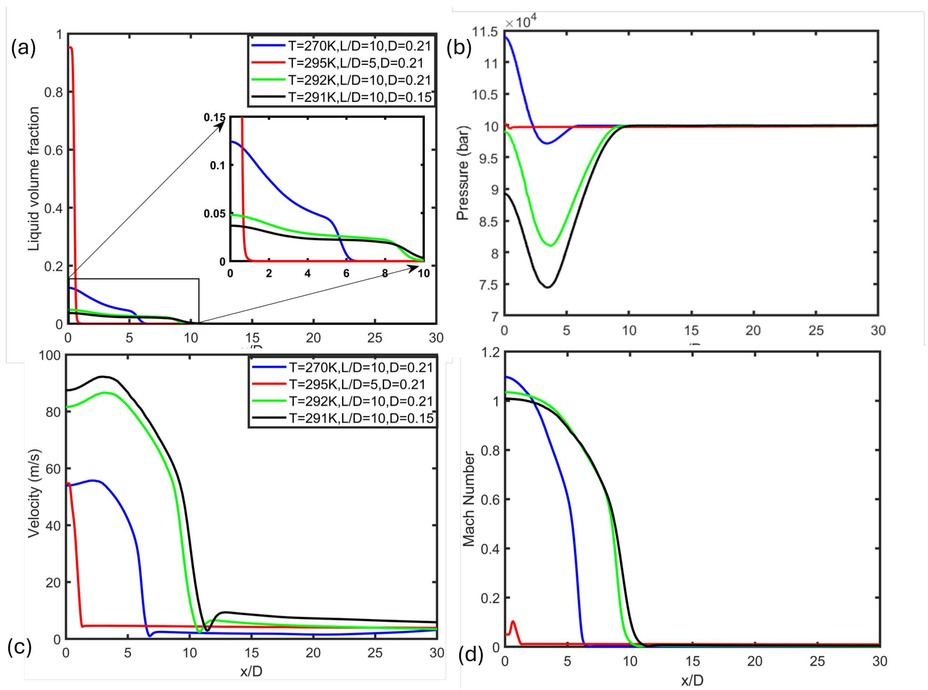

Figure 10: Radial profile of spray parameters outside nozzle at 5D (a)liquid volume fraction, (b)pressure, (c)velocity, (d) Mach number.

volume fraction is highest at the centerline, a finding that is consistent with the oblique evaporation wave (OEW) theory, which posits that the spray maintains a conical liquid core where an abrupt phase change occurs at the oblique boundary [34]. The extended liquid core observed in Case 1, compared to Cases 3 and 4, is attributed to its lower pressure ratio (R_p). This is further corroborated by the central pressure in Case 1 being considerably higher than the ambient condition (Figure 10b). Furthermore, Figures 8b and 8c reveal that the velocity is marginally lower and the pressure is higher at the spray's centre compared to the outer flow. This phenomenon is a consequence of the turning angle of the oblique evaporation wave, which results in less flow acceleration at the core at the same axial distance. At this same 5D distance, the Mach number for Cases 1, 3, and 4 approaches unity, with the distribution for Case 1 being more concentrated in the axial direction. In contrast, the pressure and velocity distributions for the non-flashing case resemble those of a conventional subcooled spray, which is characterised by a maximum axial velocity at the centerline.

Further downstream at the 10D location (Figure 11), substantial developments in the spray properties are observed. For the flashing cases, the liquid volume fraction is significantly reduced to less than 5%. Concurrently, the pressure at the centerline for Cases 3 and 4 drops to approximately half of the ambient pressure. This pressure reduction is a direct consequence of the rapid expansion from flash boiling, causing the axial front of the mixture to accelerate more rapidly than the lateral portions of the spray. A marked increase in velocity is noted between the 5D and 10D positions; the flare-flashing cases (3 and 4) accelerate by approximately 30 m/s, while the partial-flashing case (1) increases by only 10 m/s. The radial velocity profile is also inverted compared to the 5D location, with the highest velocity now occurring at the centerline. Notably, Case 4 attains the highest velocity at 10D, despite a lower initial nozzle flow rate, due to enhanced atomization from rapid bubble breakup. As seen in Figure 11(d), the mixture Mach number for all flashing sprays reaches unity at the core, indicating that the flow is sonic. However, unlike the flow in a choked single-phase nozzle, the Mach number here gradually decreases radially and then drops sharply to below 0.5 after passing through a shock wave.

The radial distribution of the liquid fraction is uniform at the 20D position (Figure 12) located downstream of the shock wave, indicating that the flash evaporation process has ended. The pressure here has recovered to ambient conditions. However, a low-pressure and low-velocity region persists at the centerline. This velocity difference is attributed to compressibility effects as the mixture traverses the shock wave. The low-pressure core can lead to vortex formation and spray contraction after the initial injection period. This behaviour is a primary differentiator between flare-flashing sprays and pressure-swirl sprays, the latter of which typically maintain a higher axial velocity. At 20D location in axial, the centerline velocities are similar across all cases. This is due to the controlled equivalent injector flow velocity and similar initial pressures in the experimental setup. The Mach number at this location stabilises at approximately 0.55 and is distributed uniformly in the radial direction.

The link between the internal flow state and the macroscopic spray morphology is visualised explicitly in the two-phase Mach

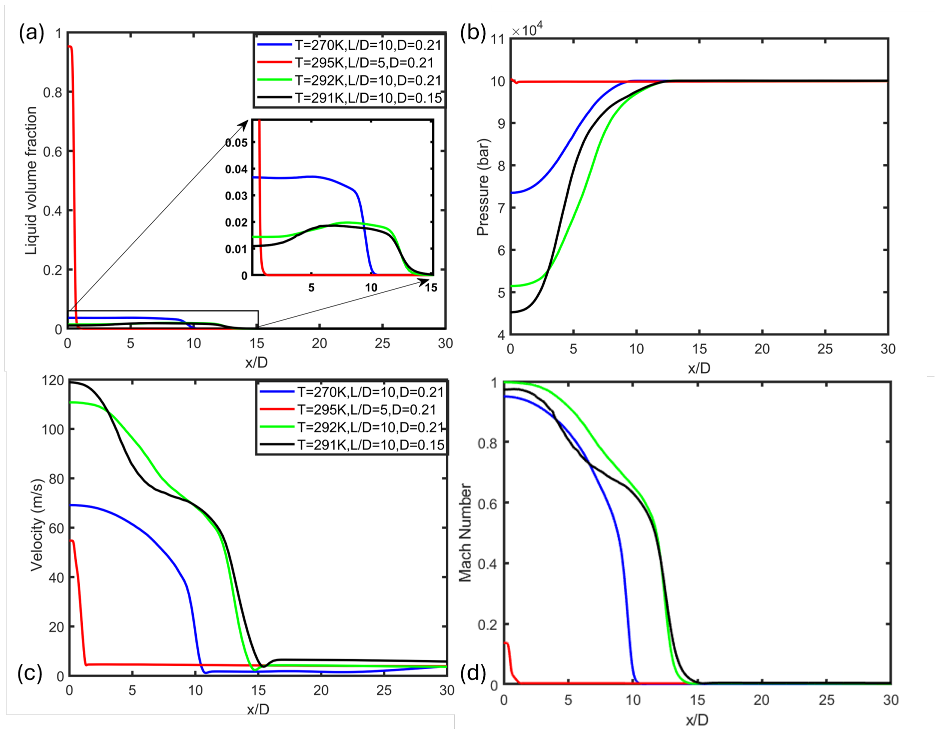

Figure 11: Radial profile of spray parameters outside nozzle at 10D (a)liquid volume fraction, (b)pressure, (c)velocity, (d) Mach number.

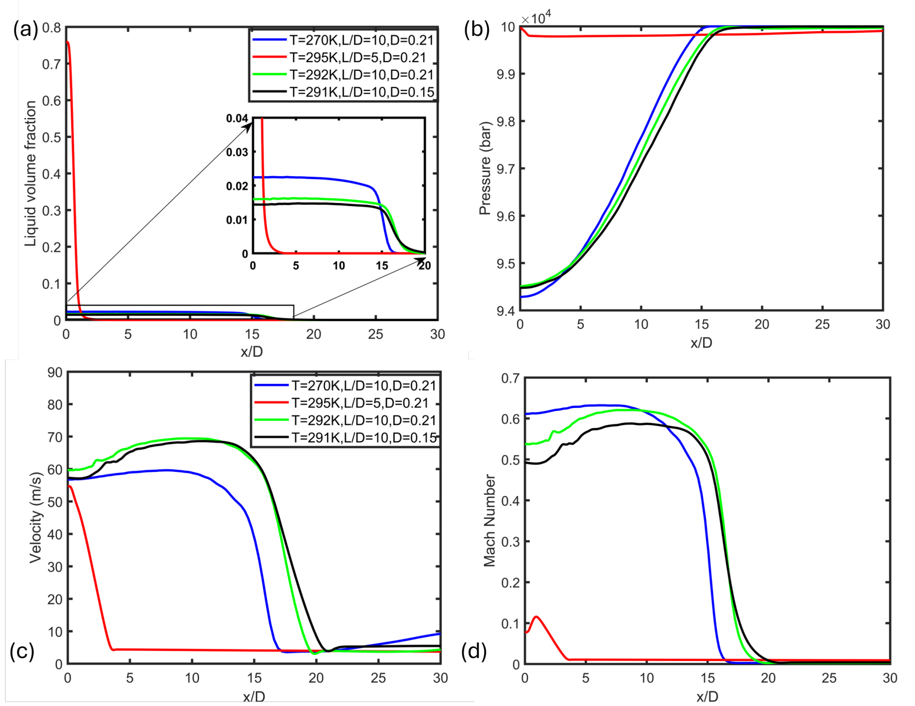

Figure 12: Radial profile of spray parameters outside nozzle at 20D (a)liquid volume fraction, (b)pressure, (c)velocity, (d) Mach number.

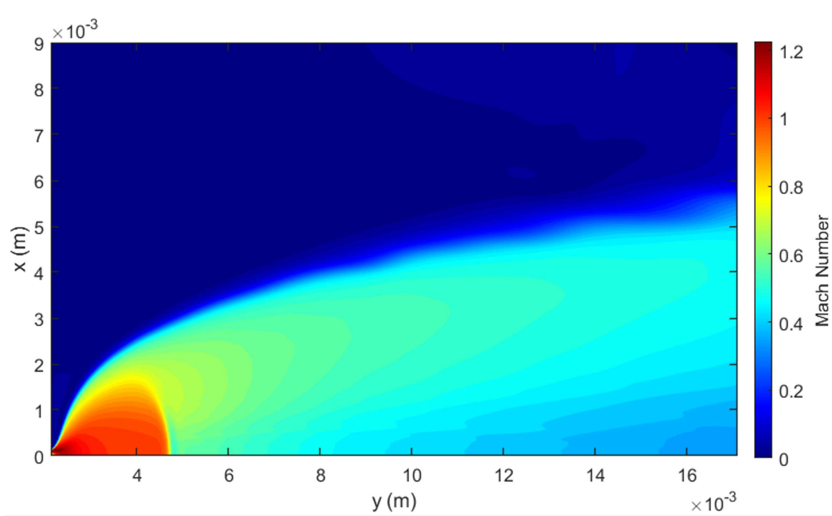

Figure 13: Mach number distribution of case 3 based on Wood's equation of mixture sound speed

number distribution presented in Figure 13. As established in the analysis of the in-nozzle flow in previous sections, the specific nozzle geometry (L/D) suppresses internal phase change while nucleating bubbles inside the nozzle, delivering a metastable, subsonic liquid jet to the nozzle exit. This subsonic exit condition with highly distributed small bubbles is the critical prerequisite for the external shock structure observed here. Upon exposure to the low-pressure ambient, the metastable liquid undergoes rapid external depressurisation and flash boiling in a homogenous condition through pre-distributed tiny bubbles. Governed by two-phase interface elasticity, the resulting generation of vapour bubbles drastically reduces the local two-phase speed of sound. The homogenous evaporation process drives the flow to supersonic speeds ($Mach > 1$)

after the oblique evaporation wave on the liquid core downstream of the orifice. The evaporation wave exceeds the local sound speed and creates a local negative pressure area (compared with ambient pressure) in the supersonic area until it hits the compression shock wave. To restore pressure equilibrium against this high-inertia central core, the stationary shock wave is forced to adapt its topology; the shock front is displaced further downstream along the centerline compared to the edges, resulting in the characteristic arc-shaped geometry rather than a planar front. On the side of this arc-shaped shock, a strong radial velocity component caused by the fast vaporisation cannot reach the local mixture sound speed in their travelling direction due to the variation of phase fraction. Therefore, travelling faster than the spray core after the normal shock wave. It is this shock-induced radial transportation structure that forces the fluid outwards. The difference between outside and inner velocity leads to the 'shrinkage' after the spray tip, which is identified in other experiments and creates the characteristic 'feather-like' spray morphology. Thus, the observed spray structure is verified to be a direct product of the coupling between the subsonic in-nozzle boundary condition and the variable-speed-of-sound gas dynamics in the near field.

3.3.4. Analysis of spray dynamics

The distinct effects of injection pressure, initial temperature, and ambient pressure were further investigated by comparing variations against the baseline Case 3 (Figure 13). Increasing the injection pressure (3.00 MPa)

Cases	6	7	8
Injection temperature (K)	292	292	300
R_p	10.5	8.3	10.6
Injection pressure (Pa)	10.9e+05	30.0e+05	10.9e+05
Ambient pressure (Bar)	0.79	1	1
Nozzle diameter (mm)	0.21	0.21	0.21
Θ_0	3.87e-07	3.87e-07	3.87e-07

Table 2: Boundary condition of additional cases with L/D ratio 10 and nozzle diameter 0.21mm.

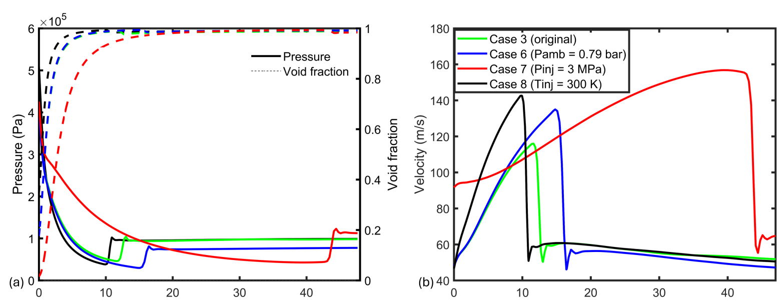

Figure 14: Pressure, void fraction, and velocity for cases 6 to 8 compared with case 3.

postpones the onset of flash boiling, consistent with previous findings [35], resulting in a higher liquid volume fraction downstream of the nozzle. This delayed phase change suggests that the mass flow rate in flare flashing is governed by a mechanism distinct from conventional nozzle choking. Conversely, elevating the initial fuel temperature (300 K) accelerates evaporation and increases spray velocity in the initial expansion region, which aligns with observations of increased in-nozzle bubble formation [13]. Interestingly, lowering the ambient pressure (0.79 Bar) to achieve a superheat degree equivalent to the high-temperature case did not yield similar behaviour. Instead, the spray characteristics mirrored the baseline Case 3 until encountering a shock wave at a different position. This comparison demonstrates that the shock wave's location is critically dependent on the pressure differential between the injection and ambient conditions, rather than on the initial fuel temperature alone, consistent with the observation in Zhang et al.[36].

The results of this study demonstrate that the structure of a flashing ammonia spray is dictated by a complex interplay between fluid thermodynamics and nozzle geometry. The HRM time scale constant, which was calibrated to match near-field spray angles at multiple downstream locations (5D, 10D, and 20D), appears to be physically correlated with the bubble nucleation process. Generally, a narrower nozzle diameter was found to promote bubble nucleation, while a shorter aspect ratio (L/D) nozzle suppressed it. This suppression of in-nozzle nucleation prevents the formation of a strong external shock wave, allowing the metastable liquid to exit the orifice at a higher velocity. The influence of operating conditions on the spray structure is multifaceted. Increasing the injection pressure primarily contributes to the spray's kinetic energy and penetration, rather than promoting in-nozzle phase change due to the finite time scale of the process. Conversely, while ambient pressure directly influences the position and structure of the downstream shock wave, it has a negligible effect on the internal nozzle flow. The initial fuel temperature governs the overall flashing intensity but has a less direct influence on the shock wave itself compared to other parameters. In summary, this work establishes that the near-field shock wave is the vital, controlling element of the ammonia flashing spray structure. This shock can be precisely manipulated not only by the fuel's thermodynamic state and ambient conditions but, critically, also by the nozzle geometry, offering a new degree of control over spray atomization and mixing.

4. Conclusion

This study investigated numerically using a two-dimensional CFD model coupled with the Homogeneous Relaxation Model (HRM) to reveal the complex physical mechanisms governing the structure of ammonia flash boiling sprays. The influence of nozzle geometry (L/D ratio, diameter) and operating conditions (R_p, injection pressure) on both the in-nozzle flow and the near-field spray development was systematically analysed. The key conclusions are as follows:

- Under flare-flashing conditions, the flow remains subsonic ($M \approx 0.3$) within the nozzle orifice. The liquid ammonia enters a metastable state, but significant phase change is suppressed until after the fluid exits the nozzle, a phenomenon consistent with experimental observations.

- The mass flow rate is not limited by sonic choking at the nozzle throat. Instead, the spray is choked by a stationary, two-phase shock wave that forms in the near-field region downstream of the nozzle. The location and strength of this shock are directly dictated by the in-nozzle exit conditions, which are in turn controlled by the nozzle geometry and operating pressures.

- A shorter L/D ratio or a wider nozzle diameter suppresses in-nozzle bubble nucleation, preventing the formation of a strong shock and leading to a higher velocity, unobstructed liquid core. Conversely, higher injection pressure increases kinetic energy and spray penetration without significantly altering the in-nozzle flashing, while lower ambient pressure primarily moves the shock front downstream.

- The near-field shock wave is the primary mechanism responsible for the spray's large-scale morphology. By inducing a deceleration and creating a pressure reduction at the spray centerline, the shock transforms the flow field. This low-velocity core, relative to the faster periphery, drives the entrainment of ambient gas and establishes a large-scale recirculating vortex, providing a comprehensive explanation for the characteristic "feather-shaped" morphology.

These findings provide a new framework for understanding flare-flashing atomisation. The realisation that a downstream shock structure controls the flow has implications for the design and optimisation of ammonia fuel injection systems. Controlling the location and strength of the shock wave presents a pathway for controlling the spray angle, penetration length, and ultimately, the fuel-air mixing process, which is crucial for efficient and stable combustion. While this 2D study establishes the fundamental mechanism, future work would extend the analysis to three-dimensional simulations to capture asymmetric instabilities and complex turbulent interactions.

5. Acknowledgements

The authors would extend their gratitude to Dr. Jan-Wilhelm Gärtner and Professor Andreas Kronenburg at the University of Stuttgart for providing the solver essential to this research.

References

[1] A. Valera-Medina, H. Xiao, M. Owen-Jones, W.I.F. David, P.J. Bowen, *Ammonia for power*, Progress in Energy and Combustion Science 69 (2018) 63–102.

[2] J. Armijo, C. Philibert, *Flexible production of green hydrogen and ammonia from variable solar and wind energy: Case study of Chile and Argentina*, International Journal of Hydrogen Energy 45 (2020) 1541–1558.

[3] E.C. Okafor, A. Hayakawa, Y. Sasaki, Y. Kitagawa, T. Kudo, A. Kurata, H. Kobayashi, *Flame stability and emissions characteristics of liquid ammonia spray co-fired with methane in a single stage swirl combustor*, Fuel 287 (2021) 119433.

[4] A. Mansour, N. Müller, *A review of flash evaporation phenomena and resulting shock waves*, Experimental Thermal and Fluid Science 107 (2019) 146–168.

[5] G. Lamanna, H. Kamoun, B. Weigand, and J. Steelant, *Towards a unified treatment of fully flashing sprays*, International Journal of Multiphase Flow 58 (2014) 168–184.

[6] M.M. Vieira, J.R. Simões-Moreira, *Low-pressure flashing mechanisms in iso-octane liquid jets*, Journal of Fluid Mechanics 572 (2007) 121–144.

[7] A.A. Avdeev, *The shape of jets during discharge of a superheated liquid (structure of wave formations and the reactive force)*, High Temperature 54 (2016) 698–707.

[8] Th. Kurschat, H. Chaves, G.E.A. Meier, *Complete adiabatic evaporation of highly superheated liquid jets*, Journal of Fluid Mechanics 236 (1992) 43–59.

[9] H. Guo, S. Zhang, M. Qenawy, L. Xu, Y. Li, *Investigation on structural characteristics of shock cells in highly superheated flash boiling jets*, Applied Thermal Engineering 278 (2025) 127370.

[10] L. Xu, Y. Li, Z.E. Liu, G. Tan, S. Shuai, H. Xu, *Effects of fuel properties on under-expansion behaviors of flash-boiling jets*, SAE Technical Paper 2023-32-0093 (2023).

[11] X. Liu, X. Yao, Z. Wang, C. Tang, *Single hole ammonia spray macroscopic and microscopic characteristics at flare and transition flash boiling regions*, Applied Thermal Engineering 235 (2023) 121443.

[12] R. Pelé, S. Bougrine, L. Blondel, B. Mattelet, B. Walter, *First Study on Ammonia Spray Characteristics with a Current GDI Engine Injector*, Fuels 2 (2021) 253–271.

[13] S. Wang, Y. Zhang, S. Qiu, D.L.S. Hung, X. Li, M. Xu, *Investigation on cavitation enhancement on flash boiling atomization using two-dimensional slit nozzles*, Energy 293 (2024) 130720.

[14] S. Li, T. Li, N. Wang, X. Zhou, R. Chen, P. Yi, *An investigation on near-field and far-field characteristics of superheated ammonia spray*, Fuel 324 (2022) 124683.

[15] S. Colson, M. Crua, M.R. Heikal, M.R. Gold, *Study on the effect of injection temperature and nozzle geometry on the flashing transition of liquid ammonia spray*, Fuel 348 (2023) 128612.

[16] Y. Fang, X. Zhang, L. Zhang, C. Lou, B. Chen, C. Zhang, *Experimental Investigation of High-Pressure Liquid Ammonia Injection under Non-Flash Boiling and Flash Boiling Conditions*, Energies 16 (2023) 2843.

[17] Z. An, J. Xing, and R. Kurose, *Numerical study on the phase change and spray characteristics of liquid ammonia flash spray*, Fuel 345 (2023) 128229.

[18] X. Chen et al., *Experimental and modeling study on liquid phase ammonia spray characteristics under high-pressure injection and engine-like ambient conditions*, International Communications in Heat and Mass Transfer 164 (2025) 108853.

[19] X. He, Y. Liu, H. Zhang, S. Bi, K. Xu, and J. Zhao, *Characteristics of high-pressure liquid ammonia sprays and combustion process in ammonia/diesel HPDI dual-fuel engines*, Journal of the Energy Institute, 120 (2025) 102059.

[20] J. Shin and S. Park, *An ammonia flash break-up model based on bubble dynamics with force and energy analysis on droplet*, Fuel 342 (2023) 127841.

[21] H. Guo, L. Nocivelli, R. Torelli, S. Som, *Towards understanding the development and characteristics of under-expanded flash boiling jets*, International Journal of Multiphase Flow 129 (2020) 103315.

[22] J.W. Gärtner, A. Kronenburg, A. Rees, J. Sender, M. Oschwald, G. Lamanna, *Numerical and experimental analysis of flashing cryogenic nitrogen*, International Journal of Multiphase Flow 130 (2020) 103360.

[23] J.W. Gärtner, A. Kronenburg, A. Rees, M. Oschwald, *Investigating 3-D Effects on Flashing Cryogenic Jets with Highly Resolved LES, Flow*, Turbulence and Combustion 111 (2023) 1175–1192.

[24] H. Guo, L. Nocivelli, R. Torelli, *Numerical study on spray collapse process of ECN spray G injector under flash boiling conditions*, Fuel 290 (2021) 119961.

[25] K. Lyras, S. Dembele, D. P. Schmidt, and J. X. Wen, *Numerical simulation of subcooled and superheated jets under thermodynamic non-equilibrium*, International Journal of Multiphase Flow 102 (2018) 16–28.

[26] J. Anez, A. Ahmed, N. Hecht, B. Duret, J. Reveillon, F.X. Demoulin, *Eulerian–Lagrangian spray atomization model coupled with interface capturing method for diesel injectors*, International Journal of Multiphase Flow 113 (2019) 325–342.

[27] C.E. Brennen, *Fundamentals of Multiphase Flow*, Cambridge University Press, Cambridge, 2005.

[28] D.L. Nguyen, *Sonic velocity in two-phase systems*, International Journal of Multiphase Flow 7 (1981) 311–320.

[29] P. Downar-Zapolski, Z. Bilicki, L. Bolle, J. Franco, *The non-equilibrium relaxation model for one-dimensional flashing liquid flow*, International Journal of Multiphase Flow 22 (1996) 473–483.

[30] J. Wang, H. Wang, Z. Zheng, M. Yao, *Numerical analysis of flash-boiling spray characteristics with liquid ammonia*, Physics of Fluids 36 (2024) 063327.

[31] S. Wu, M. Xu, D.L.S. Hung, H. Pan, *Effects of nozzle configuration on internal flow and primary jet breakup of flash boiling fuel sprays*, International Journal of Heat and Mass Transfer 110 (2017) 730–738.

[32] W. Zhong, X. Li, J. Wang, Z. Zheng, M. Yao, *Visualization study on flash boiling spray characteristics of high-pressure liquid ammonia with different nozzle diameters*, Fuel 367 (2024) 131525.

[33] H. Wu, J. Wang, Z. Zheng, H. Wang, W. Zhong, M. Yao, *Spray and evaporation characteristics of high-pressure liquid ammonia injection under flash-boiling and evaporating conditions*, Fuel 381 (2025) 133627.

[34] E. Angelo and J. R. Simões-Moreira, *Numerical Solution of Highly Expanded Flashing Liquid Jets*, Journal of Thermophysics and Heat Transfer, 21 (2007) 379–391.

[35] X. Li, J. Wang, W. Zhong, Z. Zheng, H. Wang, M. Yao, *A review on the recent advances of flash boiling atomization and combustion applications*, Progress in Energy and Combustion Science 100 (2024) 101119.

[36] J. Zhang, L. Xu, Y. Li, G. Tan, S. Shuai, H. Xu, *Characterizing under-expansion behaviors induced by rapid phase change of flash-boiling jets*, Fuel 329 (2022) 125404.

[37] Z. Zhou, J. Yin, X.-Y. Yang, B. Chen, B. Liu, *Experimental investigation on the macroscopic spray and microscopic droplet diameter, velocity and temperature of R404A flashing spray*, International Journal of Heat anbd Mass Transfer 177 (2021) 121546.

[38] S. Chen, M. Qenawy, J. Tian, *From principles to practice: Review of recent advances and perspectives in spray flash evaporation technology towards thermal management of energy systems*, Energy Conversion and Management 326 (2025) 119499.